Aqueous-Based Chemical Route toward Ambient Preparation of Multicomponent Core–Shell Nanotubes

Hui Teng Tan,[†,‡,§] Xianhong Rui,[†] Hong Yu,[†,‡] Weiling Liu,[†] Chen Xu,[†,§] Zhichuan Xu,[†] Huey Hoon Hng,[†] and Qingyu Yan[†,‡,§,*]

[†]School of Materials Science and Engineering, Nanyang Technological University, 639798 Singapore, [‡]TUM CREATE, 138602 Singapore, and [§]Energy Research Institute @ NTU, Nanyang Technological University, 637553 Singapore

ABSTRACT Room-temperature synthesized V_2O_5@MnO_2 core–shell nanotubes with tunable tunnel dimensions *via* a facile aqueous-based method are presented. The rational-designed tubular morphology endows them with good permeability of electrolyte ions for maximum utilization of the electroactive sites, while the epitaxial-grown MnO_2 imposes mechanical support to V_2O_5 against structural collapse upon long-term cycling. Hence, specific capacitance as high as 694 F g^{-1} is achieved at 1 A g^{-1} accompanied by excellent cycling stability (preserved 92% of its initial specific capacitance after 5000 cycles). In addition, functionalization of the V_2O_5@MnO_2 nanotubes with other transition metal oxides results in ternary composites, V_2O_5@MnO_2/M nanotubes (M = Fe_2O_3, Co_2O_3/$Co(OH)_2$, $Ni(OH)_2$). The versatility of this synthetic protocol provides a platform to fabricate complex ternary nanocomposites in a more benign way.

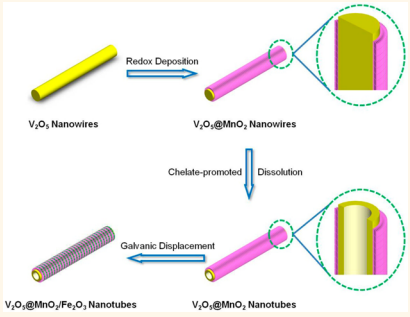

KEYWORDS: multicomponents · core–shell architecture · nanotubes · supercapacitor electrode · synergistic effect

Incompetency of conventional single-phase nanomaterials remains the cornerstone for making further technological breakthroughs. Hence, enormous progress has been made on the synthesis of nanoscale multicomponent building block with tailorable functionality. Particularly, core–shell heterostructures have been demonstrated to exhibit improved physical and chemical properties for electronics, optics, catalysis, and energy storage applications.[1−7] Many synthetic strategies for preparation of core–shell nanostructures have been demonstrated, for instance, chemical vapor deposition,[8,9] hydrothermal/solvothermal treatment,[10,11] electrodeposition,[12,13] and solution-phase route.[14−16] All of these approaches are promising to revolutionize the research field with the trend of preparing multicomponent nanostructures. However, some concerns remain: they are not easily scalable, use hazardous reactants, and operate in a less energy-efficient way. When these issues are taken into consideration, developing a new chemical route toward the preparation of multicomponent nanostructures with well-defined morphology and functionality, conducted in aqueous medium under ambient conditions, could pave a more cost-efficient and environmental benign way for high-throughput synthesis.

Multicomponent nanostructures are potential candidates for various applications, such as supercapacitor electrode materials, owing to the enhanced capacitive performance that stemmed from compensating the intrinsic shortages or synergistically combining the advantages of individual components. For example, the V_2O_5 electrode empowered the supercapacitor device with exceptionally high energy density besides having excellent rate capability with the intercalation mechanism of layered V_2O_5.[17,18] However, the structural instability of V_2O_5 has triggered a detrimental effect upon cycling. On the other hand, MnO_2 shows high cycling stability, but its energy density is not comparable to that of V_2O_5.[19,20] Thus, the combination of these two materials

* Address correspondence to alexyan@ntu.edu.sg.

Received for review February 17, 2014 and accepted March 19, 2014.

Published online March 19, 2014
10.1021/nn500942k

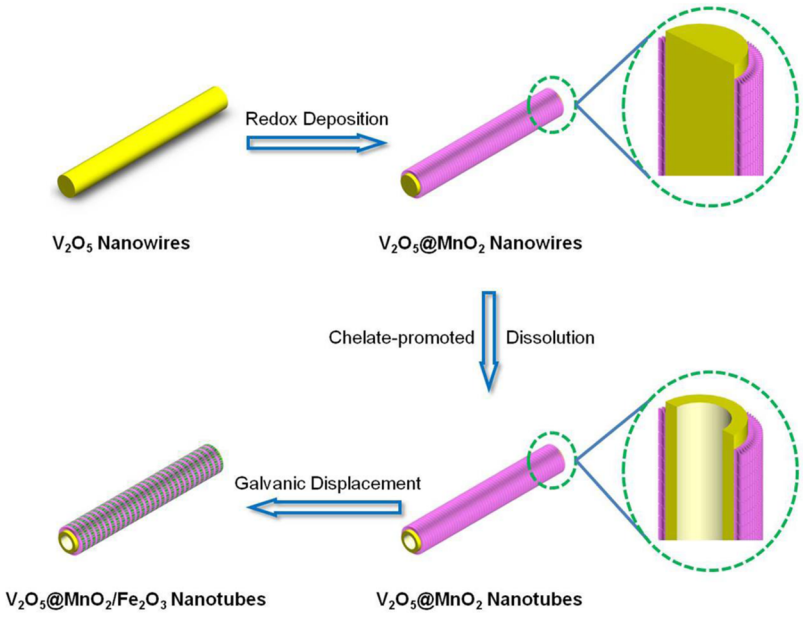

Scheme 1. Schematic representation of the proposed formation mechanism of V_2O_5@MnO_2/Fe_2O_3 core–shell nanotubes.

with rational-designed architecture might lead to unprecedented electrochemical performances, in which the conformal coating of MnO_2 on V_2O_5 imposes constraint against its structural collapse and the V_2O_5 constituent contributes to its specific capacitance and rate capability.[21,22]

Herein, we demonstrated a facile chemical route for the construction of V_2O_5@MnO_2 core–shell nanotubes with tunable diameters of V_2O_5 nanowires (ranging from 40 to 350 nm) and MnO_2 thickness in aqueous medium under ambient conditions (*e.g.*, at room temperature and 1 atm). As the formation mechanism of V_2O_5@MnO_2 nanotubes relies on the aqueous chemistry of V_2O_5 under acidic environment, the free nitrate ions released from the redox deposition of MnO_2 chelate to the V_2O_5 core to form a soluble oxonitrate complex, leading to the transformation of a solid core into a tubular structure. In this work, demonstration of the V_2O_5@MnO_2 nanotubes as the supercapacitor electrode also evidenced the practicality of multicomponent nanostructures as they outperformed their single-phase counterparts. In addition, such a green strategy could also be extended to fabricate multilayer ternary composite nanotubes (V_2O_5@MnO_2/M, M = Fe_2O_3, Co_2O_3/$Co(OH)_2$, $Ni(OH)_2$). Further functionalization of V_2O_5@MnO_2 nanotubes with other reducible transition metal oxides could be achieved by exploiting the difference in electrochemical potentials between the outermost MnO_2 layer with other foreign metal cation species in solution.[23] This preparation method opens up new avenues for scalable synthesis of multicomponent nanotubes with high tailorability in composition that are expected to hold great promise for a wide range of applications besides energy storage system.

RESULTS AND DISCUSSION

The schematic representation for the synthesis of V_2O_5@MnO_2/Fe_2O_3 multicomponent nanotubes is depicted as Scheme 1, employing an aqueous-based chemical route. The V_2O_5 with adjustable diameters was first synthesized as the scaffold for redox deposition of MnO_2 to form the V_2O_5@MnO_2 core–shell structure. Selective chelate-promoted dissolution of the V_2O_5 induced regional depletion of the core region, forming the V_2O_5@MnO_2 nanotubes. Subsequently, the realization of V_2O_5@MnO_2/Fe_2O_3 nanotubes was accomplished by the galvanic displacement reaction between the outermost layer of MnO_2 (0.91 V, MnO_2/Mn^{3+}) and the lower oxidation state Fe^{2+} (0.77 V, Fe^{3+}/Fe^{2+}) species,[24] adopting the mechanism of reductive dissolution of Mn^{3+} and the oxidative deposition of the Fe_2O_3.[23] By manipulating this chemical reaction pathway, ternary nanocomposites with disparate combination of multilayer nanotubes could be readily synthesized. In this regard, the epitaxial growth of oxide or hydroxide species on V_2O_5@MnO_2 nanotubes is highly dependent on their discrepancy in standard reduction potential with respect to MnO_2. From our preliminary results, this concept could be generalized to synthesize V_2O_5@MnO_2/Co_2O_3/$Co(OH)_2$ and V_2O_5@MnO_2/$Ni(OH)_2$ multicomponent nanotubes.

XRD analysis (Figure 1a) indicated the amorphous nature of V_2O_5@MnO_2 nanotubes by showing no significant diffraction peaks. Different from the crystalline phase of single-component V_2O_5 nanowires and MnO_2 nanoflakes (Supporting Information, Figure S1a,b), this explicit characteristic of the binary structure could be due to the amorphization of V_2O_5 under strong oxidative environment and the mild reaction conditions

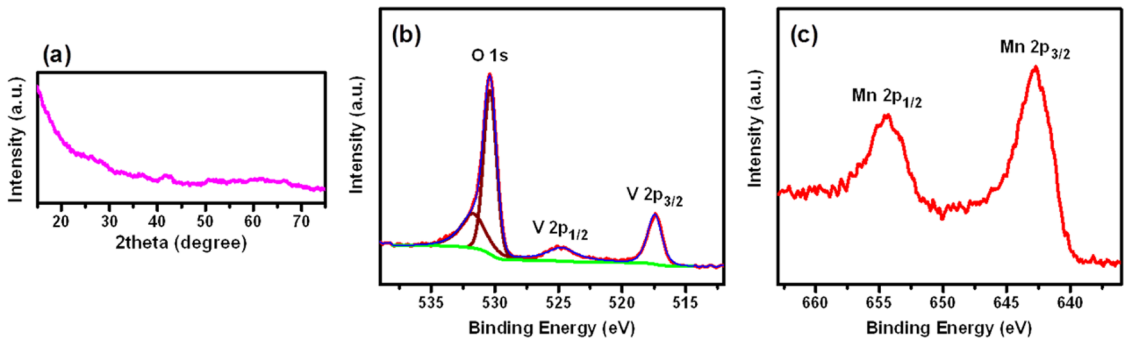

Figure 1. (a) XRD pattern; (b) XPS O 1s and V 2p core-level spectra; (c) XPS Mn 2p core-level spectrum of the V_2O_5@MnO_2 core−shell nanotubes.

attendant to the redox deposition of MnO_2. Therefore, X-ray photoelectron spectroscopy (XPS) measurement corrected using the C 1s core-level taken at 284.6 eV as the binding energy reference was conducted to further investigate the valence states of the constituents. The core binding energies of 517.4 and 524.6 eV that originated from V $2p_{3/2}$ and V $2p_{1/2}$ (Figure 1b) were in accordance with those predominant peaks of V^{5+} in V_2O_5.[25] In response to the binding energy of Mn 2p spin−orbit splitting shown in Figure 1c, Mn $2p_{3/2}$ and Mn $2p_{1/2}$ peaks located at 642.5 and 654.3 eV with spin-energy separation of 11.8 eV corresponded to Mn^{4+}.[26] The deconvolution of the O 1s peak resulted in two peaks positioned at 531.7 and 530.4 eV (Figure 1b), attributed to the existence of oxygen contents associated with the surface-absorbed hydroxyl groups and metal−oxygen bonds (Mn−O/V−O), respectively. Based on the binding energies assigned to V, Mn, and O, the compositions of the nanocomposite were proposed as V_2O_5 and MnO_2.

The low-magnification scanning electron microscopy (SEM) images shown in Figure 2a displayed densely entangled one-dimensional V_2O_5@MnO_2 nanostructures with uniform size, dominantly having microscale length (~10 μm). Successful conformal coating of the MnO_2 species could be evidenced by the rougher surface texture of the nanocomposites (inset of Figure 2a), in contrast to the smooth surface of the bare V_2O_5 nanowires (Supporting Information, Figure S1c,d), exhibiting the morphological characteristics of bare MnO_2 nanoflakes (Supporting Information, Figure S1e,f). Moreover, the radial dimension (~60−70 nm) of the nanocomposites was apparently greater the single-phase V_2O_5 nanowires (~40 nm). When the cross-sectional view of the broken interfaces was magnified, as shown in Figure 2b, the hollow interiors of the nanotubes encrusted with a flaky sheath were readily visible. Furthermore, the transmission electron microscopy (TEM) exposures disclosed a V_2O_5 hollow axial core that covered by the hierarchically assembled MnO_2 nanoflakes (Figure 2c). It was found that the tubular nanocomposite has a ~7 nm V_2O_5 inner wall thickness and a ~10 nm MnO_2 shell thickness, constructing the well-defined core−shell architecture. From the STEM/EDS (energy-dispersive X-ray spectrometry) line scan profile acquired across the core−shell nanowire (Figure 2d), both the V and Mn signals exhibited relatively high intensity at the edge region and reduced intensity at the core region, signifying the formation of tubular structure. Furthermore, Figure 2e−g illustrates the dark-field TEM image and its corresponding elemental mappings, revealing the distribution of V and Mn in a single nanocomposite. This observation was in qualitative accordance with the results obtained from the radial line scan profile (Figure 2d) that gave evidence of the epitaxially grown V_2O_5@MnO_2 core−shell nanotubes. From the Brunauer−Emmett−Teller (BET) analysis of pure MnO_2 (Supporting Information, Figure S2a), the hysteresis loop shown in the N_2 adsorption/desorption isotherm was indicative of its mesoporosity. In contrast, the absence of capillary condensation in the pure V_2O_5 isotherm (Supporting Information, Figure S2b) revealed its nonporous structure. Comparatively, V_2O_5@MnO_2 nanotubes possessed an isotherm (Supporting Information, Figure S2c) resembling pure MnO_2, which could be interpreted as having mesoporous characteristics originating from the interstices between the interconnected MnO_2 nanoparticles. The BET surface area estimated for V_2O_5@MnO_2 nanotubes could reach 191.7 $m^2\ g^{-1}$, which was apparently higher than their single-phase components, MnO_2 (71.1 $m^2\ g^{-1}$) and V_2O_5 (33.7 $m^2\ g^{-1}$).

This report also illustrates a benign chemical route for the preparation of compositionally diverse ternary tubular nanocomposites, V_2O_5@MnO_2/M (M = Fe_2O_3, Co_2O_3/$Co(OH)_2$, $Ni(OH)_2$). Using the Fe-containing nanocomposite as a demonstration, it inherited the amorphous characteristic of the V_2O_5@MnO_2 nanotubes, as shown in the XRD analysis (Figure 3a). In the XPS spectra, there was no obvious shift in binding energy illustrated in core-level spectra of V (Figure 3b) and Mn (Figure 3c) as compared to the V_2O_5@MnO_2 nanotubes. The Fe $2p_{3/2}$ and $2p_{3/2}$ peaks located at 711.5 and 724.6 eV (Figure 3d), respectively, with an associated satellite shoulders 8 eV higher than the

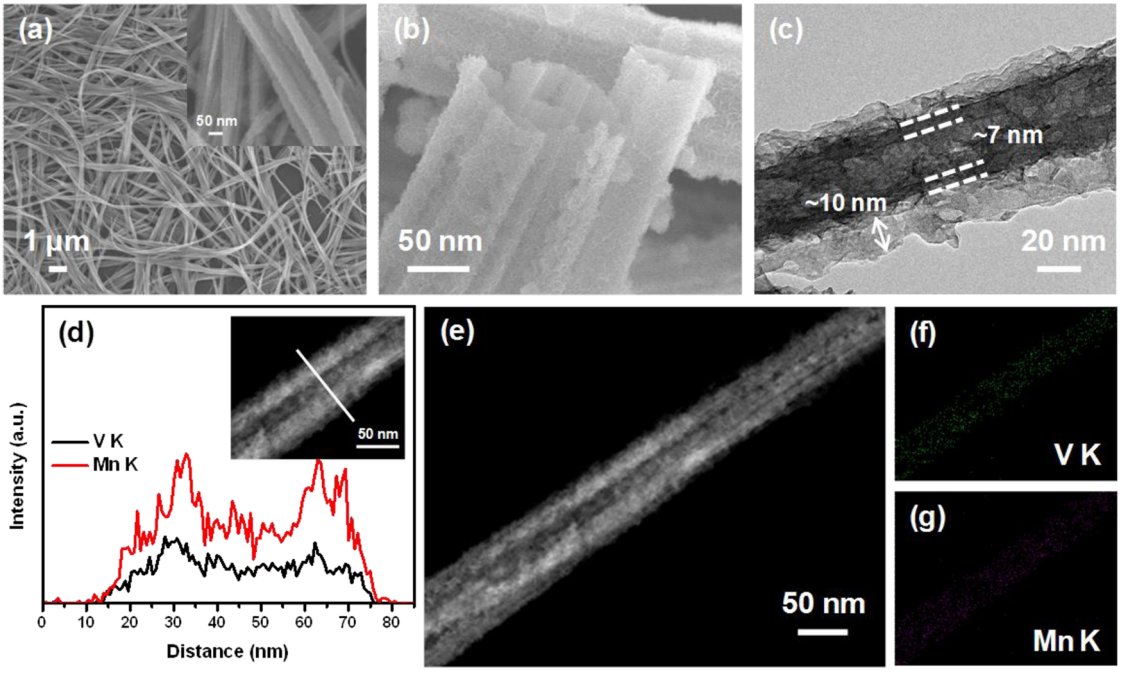

Figure 2. (a,b) SEM images, (c) TEM image, and (d) dark-field STEM/EDS line scan profile; (e–g) elemental mappings of the V_2O_5@MnO_2 core–shell nanotubes. Inset of (d) illustrates the dark-field STEM images of the V_2O_5@MnO_2 core–shell nanotubes.

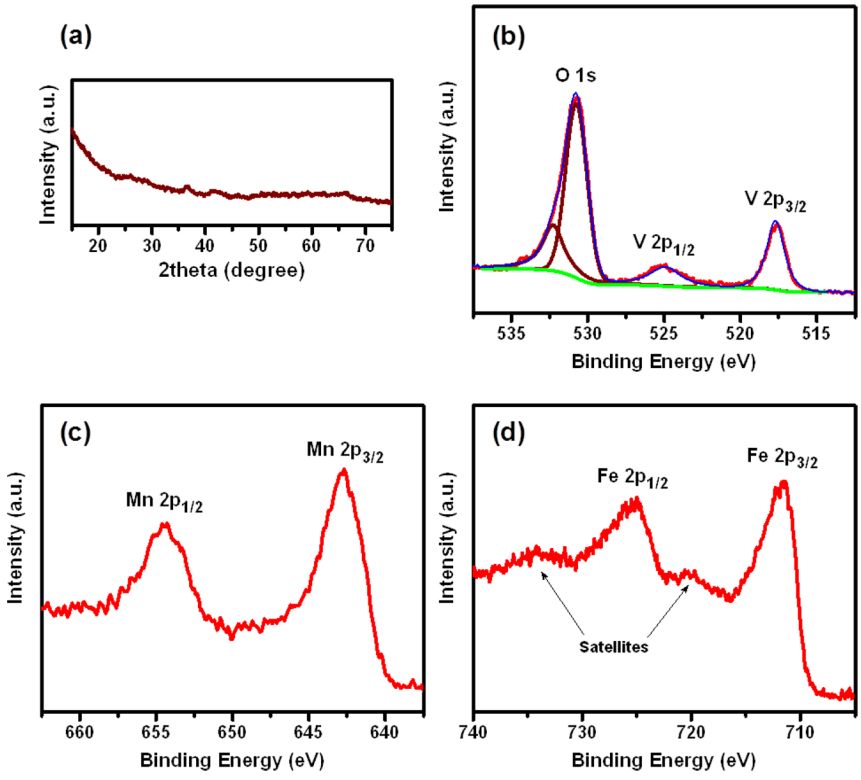

Figure 3. (a) XRD pattern; (b) XPS O 1s and V 2p core-level spectra; (c) XPS Mn 2p core-level spectrum; (d) XPS Fe 2p core-level spectrum of the V_2O_5@MnO_2/Fe_2O_3 core–shell nanotubes with the addition of $FeCl_2$ (0.1 mmol, 100 μL) precursor.

main peaks, indicated that it was trivalent Fe_2O_3.[27,28] SEM and TEM images shown in Figure 4a–c show that the surface texture, dimension, and, more importantly, the nanotube morphology of the initial V_2O_5@MnO_2 were preserved, evidencing the structural rigidity of the core–shell framework for cation substitution. The line scan profile (Figure 4d) of V_2O_5@MnO_2/Fe_2O_3 nanotubes illustrated that the emergence of the Fe

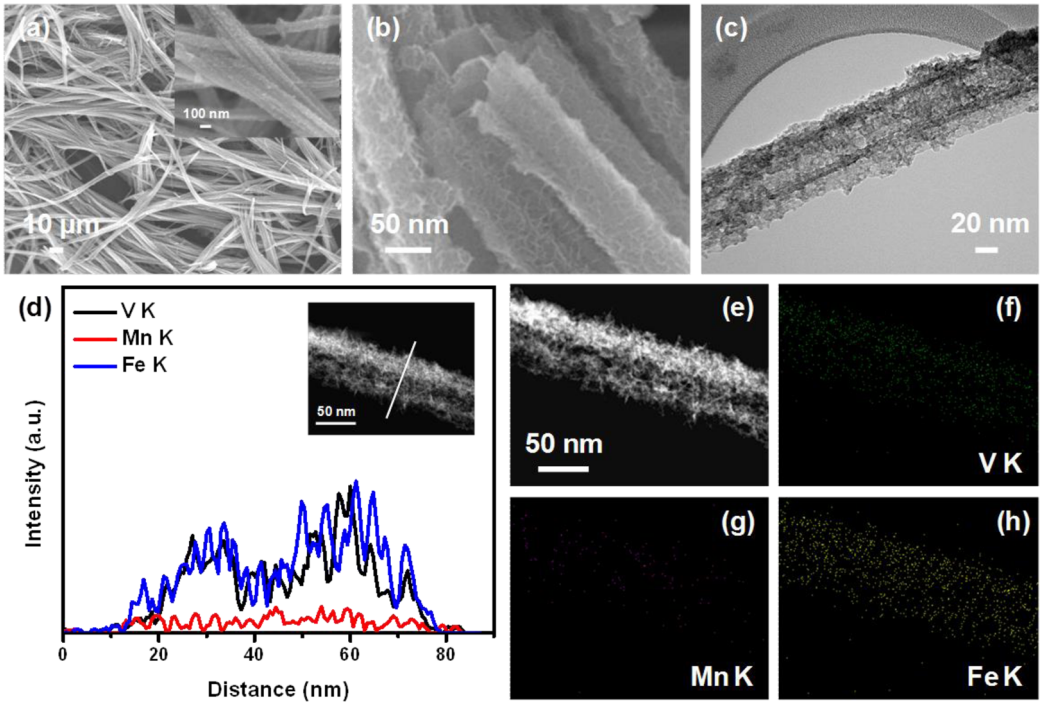

Figure 4. (a,b) SEM images, (c) TEM image, and (d) dark-field STEM/EDS line scan profile; (e–h) elemental mapping of the V_2O_5@MnO_2/Fe_2O_3 core–shell nanotubes. Inset of (d) illustrates the dark-field STEM images of the V_2O_5@MnO_2/Fe_2O_3 core–shell nanotubes.

TABLE 1. Surface Composition Derived from XPS Analysis of the As-Synthesized Samples

	surface composition (atom %)					
entry	Mn	V	Mn/V ratio	Fe	Co	Ni
V_2O_5@MnO_2 NTs	14.6	6.7	2.2			
V_2O_5@MnO_2/Fe_2O_3 0.1 mmol	3.3	6.5	0.5	8.3		
V_2O_5@MnO_2/Fe_2O_3 0.5 mmol	0.3	6.5	0.1	15		
V_2O_5@MnO_2/Co_2O_3/$Co(OH)_2$	9.4	6.7	1.4		2.7	
V_2O_5@MnO_2/$Ni(OH)_2$	13.8	6.3	2.2			3.8

TABLE 2. Element Content of the As-Synthesized Samples Derived from ICP analysis

	element content (wt %)					
entry	Mn	V	Mn/V ratio	Fe	Co	Ni
V_2O_5@MnO_2 NTs	16.87	17.29	0.976			
V_2O_5@MnO_2/Fe_2O_3 0.1 mmol	1.20	16.28	0.074	24.85		
V_2O_5@MnO_2/Fe_2O_3 0.5 mmol	0.38	16.09	0.024	37.02		
V_2O_5@MnO_2/Co_2O_3/$Co(OH)_2$	14.87	16.90	0.880		7.46	
V_2O_5@MnO_2/$Ni(OH)_2$	16.25	16.36	0.993			9.27

signal was accompanied by significant depletion of Mn concentration after the displacement of Fe^{2+} species, which was in agreement with the XPS and inductively coupled plasma (ICP) quantitative analyses summarized in Table 1 and Table 2, respectively. Additionally, the compositional mapping (Figure 4e,f) clearly depicted uniform distribution of Fe^{2+} species over the entire nanotubes. It is worth noting that the higher standard reduction potential V_2O_5 (0.95 V, V_2O_5/VO^{2+})[24] compared to the intimately contacted MnO_2 could enhance the chemical resistivity of V_2O_5 to be replaced, making the inner core layer less vulnerable to the galvanic process.

To have better illustration on the morphology evolution of the V_2O_5@MnO_2 nanotubes, V_2O_5 with larger lateral dimension, ~350 nm, was synthesized for redox deposition of MnO_2. The time-dependent kinetics shown in Scheme 2 depict the mechanistic transformation process for the nanotubes. First, solid core–shell V_2O_5@MnO_2 nanowires were formed at 0.5 h reaction duration under ambient conditions (Scheme 2a). The room-temperature heterogeneous nucleation occurred instantly on the V_2O_5 surface *via* the redox reaction between Mn^{2+} and Mn^{7+}, following the equation shown below:[29]

$$2KMnO_4 + 3Mn(NO_3)_2 + 2H_2O \rightarrow 5MnO_2 + 2KNO_3 + 4HNO_3 \quad (1)$$

As an intermediate product that formed at 3 h reaction time, the partially acidic etched core region could be clearly observed (Scheme 2b). The tubular formation could be attributed to the chelation of nitrate ions that released from the redox deposition of MnO_2 to V_2O_5 under acidic environment, yielding soluble vanadium-based oxonitrate complex, $VO_2(NO)_3$:

$$V_2O_5(s) + 2HNO_3 \rightarrow 2VO_2(NO)_3(aq) + H_2O \quad (2)$$

Extending the incubation time of the nanocomposites in solution to 9 h consequently enlarged the

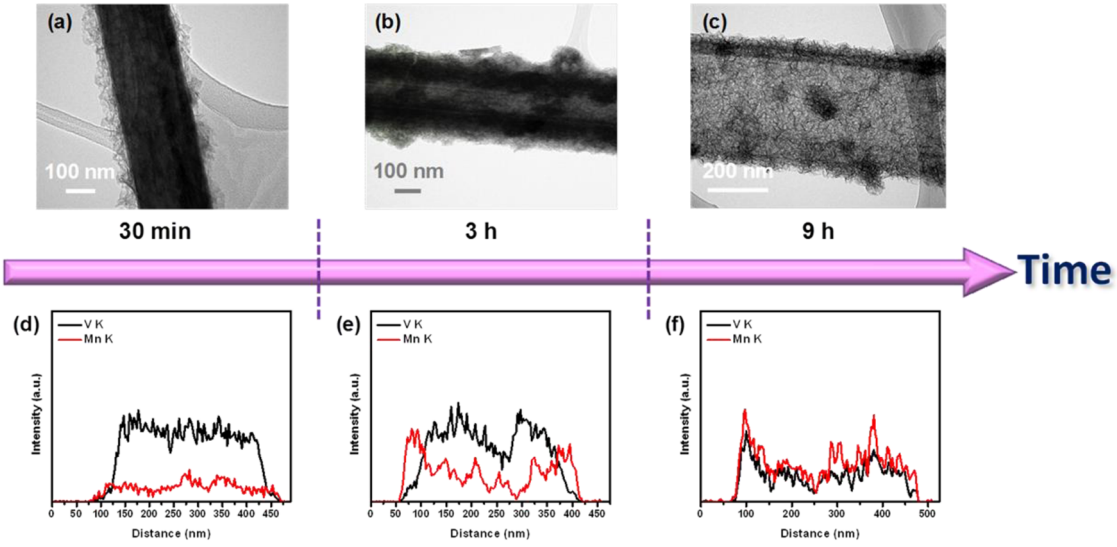

Scheme 2. Time-dependent variation of the V_2O_5@MnO_2 core−shell nanotubes and their corresponding radial STEM/EDS line scan profiles: (a,d) 30 min reaction time; (b,e) 3 h reaction time; (c,f) 9 h reaction time.

tunnel dimension of the V_2O_5 core (Scheme 2c). On the other hand, the radial line scan profiles of their corresponding nanocomposites shown in Scheme 2e,f further supported the concept that the evolution of tubular structure was started from the V_2O_5@MnO_2 solid core−shell structure to V_2O_5@MnO_2 core−shell nanotubes.

In the following step, a galvanic replacement process took place to substitute the exposed MnO_2 layer with lower oxidation state Fe^{2+} to form the V_2O_5@MnO_2/Fe_2O_3 ternary nanocomposite. The evolution of V_2O_5@MnO_2/Fe_2O_3 nanotubes was stimulated by the spontaneous oxidation−reduction reaction that was driven by the standard reduction potential difference between these two reducible species. The proposed reaction mechanism explaining that the phenomenon of oxidative precipitation of Fe species promoted the dissolution of Mn species could be further proven by a control experiment that used a high concentration of Fe^{2+}, in which almost complete depletion of the Mn species was observed and its existence could be vaguely detected by XPS measurement (Supporting Information Figure S3b). The quantitative analysis in terms of weight percentage of each component was determined by ICP measurement and is summarized in Table 2. It showed that the concentration of Mn species in 0.1 mmol V_2O_5@MnO_2/Fe_2O_3 decreased significantly as compared to the binary V_2O_5@MnO_2 nanotubes, and the Mn depletion becomes more apparent at high concentration of Fe^{2+} species, 0.5 mmol V_2O_5@MnO_2/Fe_2O_3. When this synthetic approach was extended to Co and Ni, different behaviors were observed, but both ternary nanocomposites remained in their amorphous state (Figure 5a and Figure 7a for Co and Ni, respectively). The XPS analysis of the Co-containing ternary nanocomposites revealed that the core-level of Co $2p_{3/2}$ (Figure 5d) could be deconvoluted into 2+ (781.2 eV) and 3+ (780.1 eV) oxidation states that belong to $Co(OH)_2$ and Co_2O_3, respectively.[30] In this regard, the underlying cause might be attributed to the higher standard reduction potential of the Co^{3+}/Co^{2+} pair (1.82 V),[24] resulting in competition between the hydroxide precipitation process to form $Co(OH)_2$ and the galvanic displacement process to yield Co_2O_3. This phenomenon was further proven by having a reduced amount of Mn displaced by Co species as compared to the V_2O_5@Fe_2O_3/MnO_2 ternary nanocomposite (Table 1). On the contrary, the core-level of Ni $2p_{3/2}$ with a binding energy of 855.7 eV (Figure 7d) revealed that the deposition of Ni species adopted to the hydroxide precipitation process as $Ni(OH)_2$.[31] The absence of an oxidative precipitation reaction could also be evidenced from the amount of Mn species remaining in the Ni-containing V_2O_5@MnO_2 nanocomposite shown in Table 1, preserving almost the same amount of Mn species as the V_2O_5@MnO_2 nanotubes. Hence, we proposed that a successful galvanic displacement reaction can only be achieved by having suitable redox potential; otherwise, the hydroxide precipitation will become the predominant process. The ICP results summarized in Table 2 revealed that the concentration of Mn decreased after the addition of Fe and Co and remained almost the same after the addition of Ni, showing similar trend as the XPS analysis. On the other hand, the ICP results also showed that the V species is relatively inert toward the galvanic replacement process. It is worth noting that the tubular core−shell architecture pertained to the Co- and Ni-containing ternary nanocomposites with only compositional changes at the outermost layer (Figure 6a−h and Figure 8a−h for Co and Ni, respectively). This chemical route illustrated the versatility of an aqueous-based synthetic protocol for accessing well-defined morphology with tunable composition.

As a demonstration of potential applications, the V_2O_5@MnO_2 nanotubes were tested as the supercapacitor

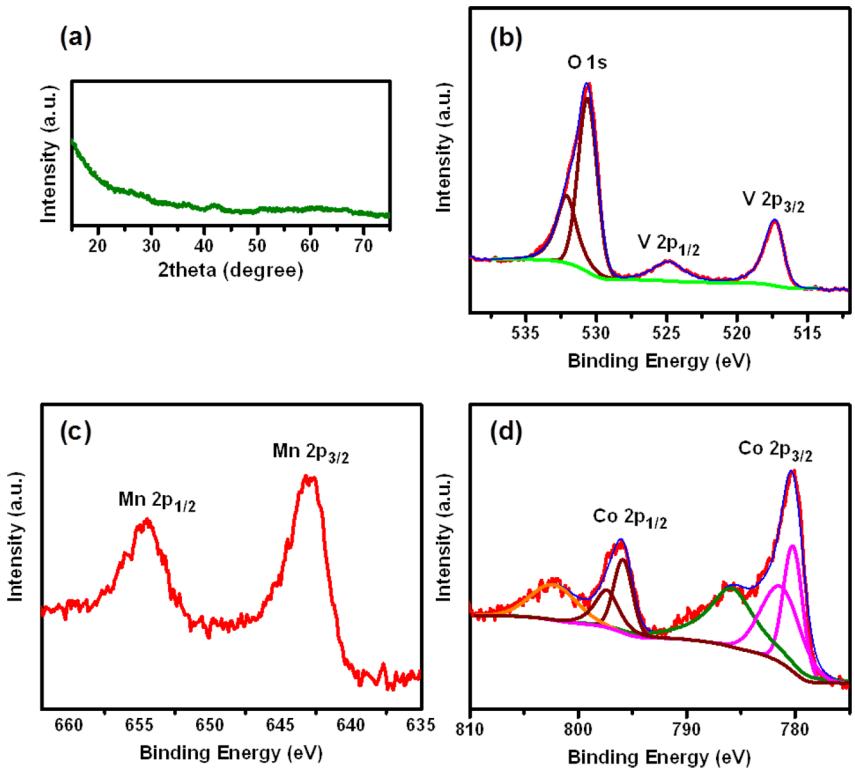

Figure 5. (a) XRD pattern; (b) XPS O 1s and V 2p core-level spectra; (c) XPS Mn 2p core-level spectrum; (d) XPS Co 2p core-level spectrum of the V_2O_5@MnO_2/Co_2O_3/$Co(OH)_2$ core−shell nanotubes with the addition of $CoCl_2$ (0.1 mmol, 200 μL) precursor.

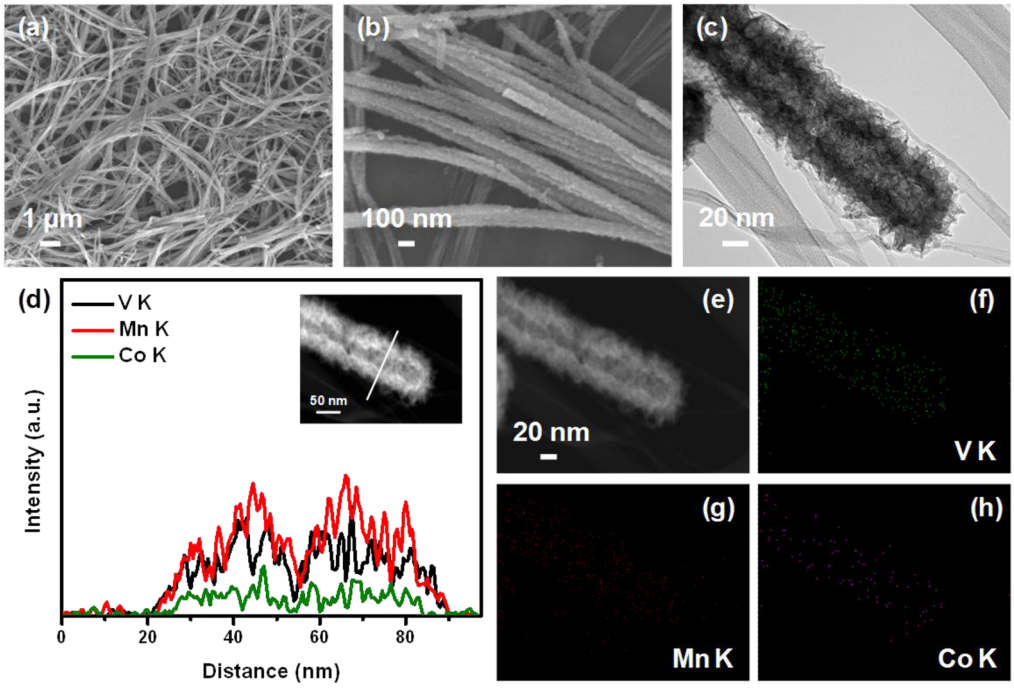

Figure 6. (a,b) SEM images, (c) TEM image, and (d) dark-field STEM/EDS line scan profile; (e−h) elemental mapping of the V_2O_5@MnO_2/Co_2O_3/$Co(OH)_2$ core−shell nanotubes. Inset of (d) illustrates the dark-field STEM image of the V_2O_5@MnO_2/Co_2O_3/$Co(OH)_2$ core−shell nanotubes.

electrode. The cyclic voltammetry (CV) curve of the V_2O_5@MnO_2 nanotubes obtained at 2 mV s^{-1} (Figure 9a) in Na_2SO_4 aqueous electrolyte exhibited a symmetrical rectangular shape coupled with a pair of V_2O_5 redox peaks (−0.18/0.17 V), indicating the ideal capacitive behavior of the nanocomposite.[32,33] Along with this line, cyclic voltammetric investigation of V_2O_5@MnO_2 nanotubes at 100 mV s^{-1} indicated its excellent kinetic

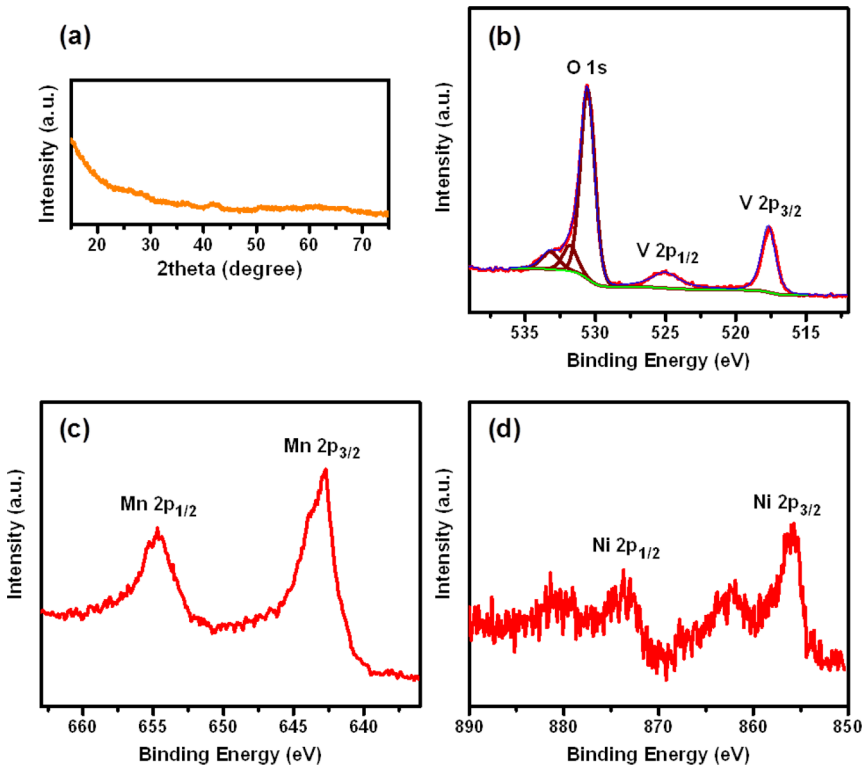

Figure 7. (a) XRD pattern; (b) XPS O 1s and V 2p core-level spectra; (c) XPS Mn 2p core-level spectrum; (d) XPS Ni 2p core-level spectrum of the V_2O_5@ V_2O_5@MnO_2/$Ni(OH)_2$ core–shell nanotubes with the addition of $NiCl_2$ (0.1 mmol, 200 μL) precursor.

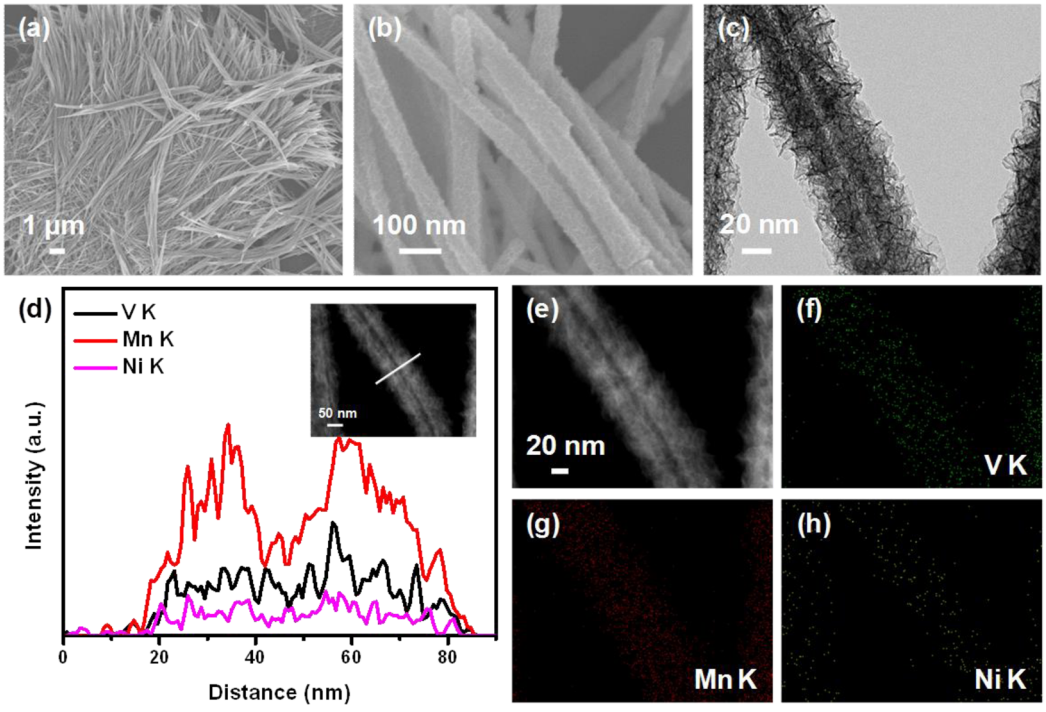

Figure 8. (a,b) SEM images, (c) TEM image, and (d) dark-field STEM/EDS line scan profile; (e–h) elemental mapping of the V_2O_5@MnO_2/$Ni(OH)_2$ core–shell nanotubes. Inset of (d) illustrates the dark-field STEM image of the V_2O_5@MnO_2/$Ni(OH)_2$ core–shell nanotubes.

reversibility by attaining an almost rectangular CV loop without significant distortion (Figure 9b). On one hand, the specific capacitance evaluated by galvanic charge/discharge measurement (Figure 9c) at 1 A g^{-1} for the pure V_2O_5 nanowires, pure MnO_2 nanoflakes, and V_2O_5@MnO_2 nanotubes was 503, 304, and 694 F g^{-1}, respectively, in which the V_2O_5@MnO_2 nanotubes exhibited superior capacitive capabilities to those of

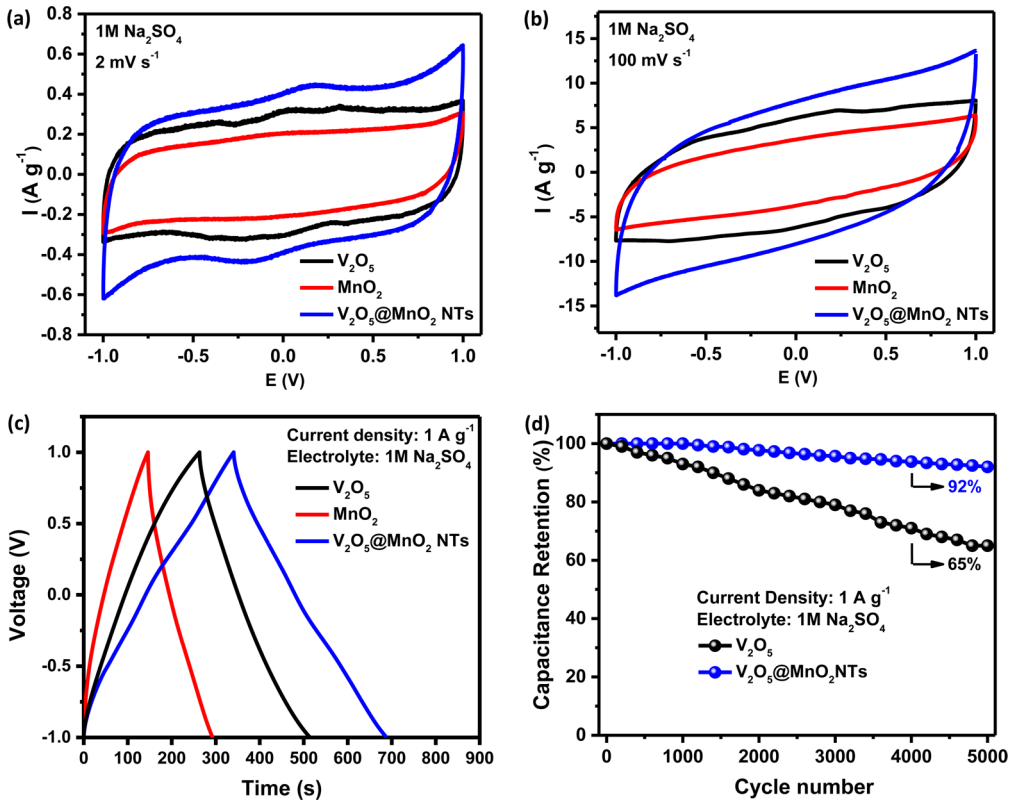

Figure 9. Electrochemical measurements of the as-prepared samples: cyclic voltammogram of the as-prepared samples at a scan rate of (a) 2 mV s^{-1} and (b) 100 mV s^{-1}. (c) Galvanic charged/discharged curves at current density of 1 A g^{-1}. (d) Cycling performance.

single-phase V_2O_5 and MnO_2 nanoflakes. Furthermore, the V_2O_5@MnO_2 nanotubes inherited the good cycling stability of MnO_2 that retained 92% of its original specific capacitance after 5000 cycles, surpassing V_2O_5 that undergoes rapid capacitive fading upon cycling (Figure 9d). On the other hand, V_2O_5@MnO_2 nanotubes could achieve 614, 530, and 414 F g^{-1} at current densities of 2, 3, and 5 A g^{-1}, respectively (Supporting Information, Figure S4a). The overall electrochemical performance of the V_2O_5@MnO_2 nanotubes could be clearly visualized from the Ragone plot (Supporting Information, Figure S4b). Remarkably, power density as high as 5 kW kg^{-1} was obtained while maintaining energy density of 43 W h kg^{-1}, suggesting that it holds great promise toward practical implementation in supercapacitors. Here, the electrochemical performances examined for the V_2O_5@MnO_2 nanotubes exhibited distinguishable properties over conventional single-phase counterparts from different aspects. The observed electrochemical enhancement in terms of specific capacitance could be attributed to the successful tailoring of morphological and interfacial properties of the V_2O_5@MnO_2 nanotubes, endowing them with higher specific BET surface area as compared to their single-phase V_2O_5 and MnO_2. With the unique hollow architecture, easy penetration and excellent accessibility of electrolyte were guaranteed for both MnO_2 and V_2O_5, maximizing the electroactive surface area and leading to optimum electrochemical performances. On the other hand, the design rationale for a tubular V_2O_5@MnO_2 core–shell nanostructure was able to impose constraint against structural collapse of V_2O_5 by having a conformal coating of MnO_2 on its surface while the protected V_2O_5 can exhibit higher specific capacitance and excellent electrochemical performance at high rate measurement.

CONCLUSIONS

In summary, V_2O_5@MnO_2 nanotubes were successfully synthesized using a scalable approach under ambient conditions. In addition, the well-defined morphology but adaptive dimension of the V_2O_5@MnO_2 nanotubes could be tuned to meet the requirements of different applications. From a fundamental point of view, the mechanism for the transformation of solid to hollow core–shell structure could be attributed to the formation of a soluble oxonitrate complex of vanadium upon redox deposition of MnO_2. Notably, a facile aqueous-based synthetic protocol for accessing tubular ternary nanocomposites with tunable chemical compositions was also developed. The preliminary results manifested the versatility of this aqueous-based chemical route for expanding the binary V_2O_5@MnO_2 nanotubes to the tubular V_2O_5@MnO_2/M (M = Fe_2O_3, Co_2O_3/$Co(OH)_2$, $Ni(OH)_2$)

ternary composite. In addition, the successful attempt at applying the multicomponent V_2O_5@MnO_2 nanotubes as supercapacitor electrodes has prompted this synthetic strategy to be implemented to other combinations of materials used for a wide range of applications.

EXPERIMENTAL METHODS

Synthesis of V_2O_5@MnO_2 Core−Shell Structures. V_2O_5 (2 mmol, 2 mL) solution was extracted and mixed with deionized water (30 mL). $Mn(NO_3)_2 \cdot 4H_2O$ (0.1 mmol, 1.8 mL) and $KMnO_4$ (0.1 mmol, 1.2 mL) solutions were then added sequentially. The mixture was stirred at room temperature for 0.5 and 3 h to obtain solid and hollow core−shell structures, respectively.

Synthesis of V_2O_5@MnO_2/M Heterostructures. Since the synthesis of tubular V_2O_5@MnO_2/M heterostructures was similar, V_2O_5@MnO_2/Fe_2O_3 nanotubes were used for the demonstration. Solution of V_2O_5@MnO_2 nanotubes (1 mmol, 1 mL) was extracted and mixed with deionized water (5 mL). Anhydrous $FeCl_2$ (0.1 mmol, 100 μL) was added dropwise into the V_2O_5@MnO_2 nanotube solution and stirred at 80 °C for 1 h. Subsequently, the mixture was washed three times with deionized water and dried in a vacuum oven overnight. For the synthesis of V_2O_5@MnO_2/Co_2O_3/$Co(OH)_2$ and V_2O_5@MnO_2/$Ni(OH)_2$, anhydrous $CoCl_2$ (0.1 mmol, 200 μL) and $NiCl_2$ (0.1 mmol, 200 μL) were used, respectively, while the reaction conditions were otherwise identical to the synthesis of V_2O_5@MnO_2/Fe_2O_3.

Material Characterization. X-ray diffraction (XRD) was performed on Shimadzu thin film diffractometer with Cu Kα radiation (λ = 0.15406 nm) for compositional analysis. The diffraction pattern was collected within 10−70° (2θ). JEOL JSM-7600F scanning electron spectroscopy was used for morphology investigation. A JEOL JEM 2100 transmission electron microscope, operating at 200 kV, was employed for high-resolution TEM imaging, and dark-field scanning transmission electron microscopy was used to perform the energy-dispersive X-ray spectrometry elemental mapping and line scan analyses. X-ray photoelectron spectroscopy measurements were performed on VG Escalab 250 spectrometer using Al Kα 1846.6 eV anode. The binding energy was calibrated using the C 1s peak at 284.6 eV as the reference. An accelerated surface area and porosimetry system (ASAP 2020) was used for the measurement of nitrogen adsorption/desorption isotherms at −196 °C. Before the measurement, all as-prepared samples were degassed at 150 °C for 6 h under vacuum. The specific surface areas were determined by the Brunauer−Emmett−Teller method. The metal content was measured by inductively coupled plasma analysis using a dual-view Optima 5300 DV ICP-OES system. Mixture of nitric acid and hydrochloric acid was used to dissolve the sample prior to the measurement.

Electrochemical Characterization. The electrochemical characterizations were carried out on Solartron analytical equipment (model 1470E). Double-electrode cell configurations were employed in cyclic voltammetry, galvanostatic charge/discharge voltammetry. A slurry that consisted of active materials, SWNTs and PVDF binder in a ratio of 7:2:1, was mechanically stirred for 1 day before pasting on a carbon paper current collector. Finally, the electrodes were dried in a 50 °C vacuum oven overnight to evaporate the solvent. Na_2SO_4 was used as the electrolyte for the two- and three-electrode cell configurations.

The specific capacitance of the cell is derived from the galvanostatic charge/discharge curve using the following equation:

$$C_{\text{hybrid}} = \left(\frac{I}{-m\dfrac{dV}{dt}} \right) \tag{3}$$

where I is the discharge current, dV/dt is the slope of the discharged curve after IR drop, and m is the total mass of the active materials. For the symmetry electrode configuration, the single-electrode capacitance is calculated according to $C_{sc} = 4C_{\text{hybrid}}$.

The energy (E) and power (P) density can be calculated by using eqs 4 and 5, respectively.

$$E(\text{Whkg}^{-1}) = \frac{1}{2} C_{\text{hybrid}} (\Delta V)^2 \times \frac{1000}{3600} \tag{4}$$

$$P(\text{Wkg}^{-1}) = \frac{E}{\Delta t} \times 3600 \tag{5}$$

where C_{hybrid}, ΔV, and Δt are the specific capacitance of the cell, voltage range, and discharged time after the IR drop, respectively.

Conflict of Interest: The authors declare no competing financial interest.

Acknowledgment. We gratefully acknowledge Singapore MOE AcRF Tier 1 Grants RG2/13, A*STAR SERC Grant 1021700144, Singapore MPA 23/04.15.03 grant, and Singapore National Research Foundation under CREATE program: EMobility in Megacities.

Supporting Information Available: Experimental method for the synthesis of single-phase V_2O_5 and MnO_2, XRD analysis and SEM images the single-phase V_2O_5 and MnO_2, N_2 absorption/desorption isotherms, XPS analysis, and electrochemical performances of the as-prepared samples. This material is available free of charge *via* the Internet at http://pubs.acs.org.

REFERENCES AND NOTES

1. Zhang, Y.; Suenaga, K.; Colliex, C.; Iijima, S. Coaxial Nanocable: Silicon Carbide and Silicon Oxide Sheathed with Boron Nitride and Carbon. *Science* **1998**, *281*, 973–975.
2. Taberna, P. L.; Mitra, S.; Poizot, P.; Simon, P.; Tarascon, J. M. High Rate Capabilities Fe_3O_4-Based Cu Nano-architectured Electrodes for Lithium-Ion Battery Applications. *Nat. Mater.* **2006**, *5*, 567–573.
3. Lai, X.; Halpert, J. E.; Wang, D. Recent Advances in Micro-/Nano-structured Hollow Spheres for Energy Applications: From Simple to Complex Systems. *Energy Environ. Sci.* **2012**, *5*, 5604–5618.
4. Liu, Y.; Tang, Z. Multifunctional Nanoparticle@MOF Core−Shell Nanostructures. *Adv. Mater.* **2013**, *25*, 5819–5825.
5. Lyon, J. L.; Fleming, D. A.; Stone, M. B.; Schiffer, P.; Williams, M. E. Synthesis of Fe Oxide Core/Au Shell Nanoparticles by Iterative Hydroxylamine Seeding. *Nano Lett.* **2004**, *4*, 719–723.
6. Hou, Y.; Cheng, Y.; Hobson, T.; Liu, J. Design and Synthesis of Hierarchical MnO_2 Nanospheres/Carbon Nanotubes/Conducting Polymer Ternary Composite for High Performance Electrochemical Electrodes. *Nano Lett.* **2010**, *10*, 2727–2733.
7. Zhou, S.; Varughese, B.; Eichhorn, B.; Jackson, G.; McIlwrath, K. Pt−Cu Core−Shell and Alloy Nanoparticles for Heterogeneous NOx Reduction: Anomalous Stability and Reactivity of a Core−Shell Nanostructure. *Angew. Chem., Int. Ed.* **2005**, *44*, 4539–4543.
8. Peng, H.; Xie, C.; Schoen, D. T.; McIlwrath, K.; Zhang, X. F.; Cui, Y. Ordered Vacancy Compounds and Nanotube Formation in $CuInSe_2$−CdS Core−Shell Nanowires. *Nano Lett.* **2007**, *7*, 3734–3738.
9. Ben-Ishai, M.; Patolsky, F. A Route to High-Quality Crystalline Coaxial Core/Multishell Ge@Si$(GeSi)_n$ and Si@$(GeSi)_n$ Nanowire Heterostructures. *Adv. Mater.* **2010**, *22*, 902–906.
10. Qin, Y.; Wang, X.; Wang, Z. L. Microfibre−Nanowire Hybrid Structure for Energy Scavenging. *Nature* **2008**, *451*, 809–813.

11. Xia, X.; Chao, D.; Qi, X.; Xiong, Q.; Zhang, Y.; Tu, J.; Zhang, H.; Fan, H. J. Controllable Growth of Conducting Polymers Shell for Constructing High-Quality Organic/Inorganic Core/Shell Nanostructures and Their Optical-Electrochemical Properties. *Nano Lett.* **2013**, *13*, 4562–4568.
12. Saadat, S.; Zhu, J.; Sim, D. H.; Hng, H. H.; Yazami, R.; Yan, Q. Coaxial Fe_3O_4/CuO Hybrid Nanowires as Ultra Fast Charge/Discharge Lithium-Ion Battery Anodes. *J. Mater. Chem. A* **2013**, *1*, 8672–8678.
13. Li, Q.; Wang, Z. L.; Li, G. R.; Guo, R.; Ding, L. X.; Tong, Y. X. Design and Synthesis of MnO_2/Mn/MnO_2 Sandwich-Structured Nanotube Arrays with High Supercapacitive Performance for Electrochemical Energy Storage. *Nano Lett.* **2012**, *12*, 3803–3807.
14. Mazumder, V.; Chi, M.; More, K. L.; Sun, S. Synthesis and Characterization of Multimetallic Pd/Au and Pd/Au/FePt Core/Shell Nanoparticles. *Angew. Chem., Int. Ed.* **2010**, *49*, 9368–9372.
15. Liu, Y. H.; Wang, F.; Hoy, J.; Wayman, V. L.; Steinberg, L. K.; Loomis, R. A.; Buhro, W. E. Bright Core−Shell Semiconductor Quantum Wires. *J. Am. Chem. Soc.* **2012**, *134*, 18797–18803.
16. Goebl, J. A.; Black, R. W.; Puthussery, J.; Giblin, J.; Kosel, T. H.; Kuno, M. Solution-Based II−VI Core/Shell Nanowire Heterostructures. *J. Am. Chem. Soc.* **2008**, *130*, 14822–14833.
17. Chen, Z.; Augustyn, V.; Wen, J.; Zhang, Y.; Shen, M.; Dunn, B.; Lu, Y. High-Performance Supercapacitors Based on Intertwined CNT/V_2O_5 Nanowire Nanocomposites. *Adv. Mater.* **2011**, *23*, 791–795.
18. Qu, Q.; Zhu, Y.; Gao, X.; Wu, Y. Core−Shell Structure of Polypyrrole Grown on V_2O_5 Nanoribbon as High Performance Anode Material for Supercapacitors. *Adv. Energy Mater.* **2012**, *2*, 950–955.
19. Lu, X.; Zhai, T.; Zhang, X.; Shen, Y.; Yuan, L.; Hu, B.; Gong, L.; Chen, J.; Gao, Y.; Zhou, J.; *et al.* WO_{3-x}@Au@MnO_2 Core−Shell Nanowires on Carbon Fabric for High-Performance Flexible Supercapacitors. *Adv. Mater.* **2012**, *24*, 938–944.
20. Chen, L. F.; Huang, Z. H.; Liang, H. W.; Guan, Q. F.; Yu, S. H. Bacterial-Cellulose-Derived Carbon Nanofiber@MnO_2 and Nitrogen-Doped Carbon Nanofiber Electrode Materials: An Asymmetric Supercapacitor with High Energy and Power Density. *Adv. Mater.* **2013**, *25*, 4746–4752.
21. Mai, L.; Dong, F.; Xu, X.; Luo, Y.; An, Q.; Zhao, Y.; Pan, J.; Yang, J. Cucumber-like V_2O_5/Poly(3,4-ethylenedioxythiophene)&MnO_2 Nanowires with Enhanced Electrochemical Cyclability. *Nano Lett.* **2013**, *13*, 740–745.
22. Xie, X. Y.; Liu, W. W.; Zhao, L. Y.; Huang, C. D. Structural and Electrochemical Behavior of Mn-V Oxide Synthesized by a Novel Precipitation Method. *J. Solid State Electrochem.* **2010**, *14*, 1585–1594.
23. Oh, M. H.; Yu, T.; Yu, S. H.; Lim, B.; Ko, K. T.; Willinger, M. G.; Seo, D. H.; Kim, B. H.; Cho, M. G.; Park, J. H.; *et al.* Galvanic Replacement Reactions in Metal Oxide Nanocrystals. *Science* **2013**, *340*, 964–968.
24. Haynes, W. M. *CRC Handbook of Chemistry and Physics*, 93rd ed.; CRC Press: Boca Raton, FL, 2012.
25. Sathiya, M.; Prakash, A. S.; Ramesha, K.; Tarascon, J. M.; Shukla, A. K. V_2O_5-Anchored Carbon Nanotubes for Enhanced Electrochemical Energy Storage. *J. Am. Chem. Soc.* **2011**, *133*, 16291–16299.
26. Subramanian, V.; Zhu, H.; Vajtai, R.; Ajayan, P. M.; Wei, B. Hydrothermal Synthesis and Pseudocapacitance Properties of MnO_2 Nanostructures. *J. Phys. Chem. B* **2005**, *109*, 20207–20214.
27. Oscarson, D. W.; Huang, P. M.; Defosse, C.; Herbillon, A. Oxidative Power of Mn(IV) and Fe(III) Oxides with Respect to As(III) in Terrestrial and Aquatic Environments. *Nature* **1981**, *291*, 50–51.
28. Yamashita, T.; Hayes, P. Analysis of XPS Spectra of Fe^{2+} and Fe^{3+} Ions in Oxide Materials. *Appl. Surf. Sci.* **2008**, *254*, 2441–2449.
29. Wang, X.; Li, Y. Synthesis and Formation Mechanism of Manganese Dioxide Nanowires/Nanorods. *Chem.—Eur. J.* **2003**, *9*, 300–306.
30. Tan, B. J.; Klabunde, K. J.; Sherwood, P. M. A. XPS Studies of Solvated Metal Atom Dispersed (SMAD) Catalysts. Evidence for Layered Cobalt-Manganese Particles on Alumina and Silica. *J. Am. Chem. Soc.* **1991**, *113*, 855–861.
31. Venezia, A. M.; Bertoncello, R.; Deganello, G. X-ray Photoelectron Spectroscopy Investigation of Pumice-Supported Nickel Catalysts. *Surf. Interface Anal.* **1995**, *23*, 239–247.
32. Augustyn, V.; Come, J.; Lowe, M. A.; Kim, J. W.; Taberna, P. L.; Tolbert, S. H.; Abruña, H. D.; Simon, P.; Dunn, B. High-Rate Electrochemical Energy Storage through Li^+ Intercalation Pseudocapacitance. *Nat. Mater.* **2013**, *12*, 518–522.
33. Lang, X.; Hirata, A.; Fujita, T.; Chen, M. Nanoporous Metal/Oxide Hybrid Electrodes for Electrochemical Supercapacitors. *Nat. Nanotechnol.* **2011**, *6*, 232–236.